Application of a Hybrid Discontinuous Galerkin Scheme onto Quantum-Liouville-type Equations for Heterostructure Devices

1st Valmir Ganiu 🄳
Chair for High Frequency Techniques, TU Dortmund
Dortmund, Germany
valmir.ganiu@tu-dortmund.de

2nd Dirk Schulz 🄳
Chair for High Frequency Techniques, TU Dortmund
Dortmund, Germany
dirk2.schulz@tu-dortmund.de

Abstract—In addition to the high accuracy nature of conventional finite element formalisms, discontinuous Galerkin methods are suited for the realization of high performance computing. Therefore, this approach is applied onto the Liouville-von Neumann equation describing the electron transport in nanoscale heterostructure devices. Unfortunately, discontinuous Galerkin methods are prone to instability issues. As demonstrated, these inherent stability issues of the discontinuous Galerkin method can be alleviated by the use of a complex absorbing potential ensuring an efficient use of the Liouville-von Neumann equation.

I. INTRODUCTION

With limited time and hardware resources, software optimization is mandatory for carrier transport simulations within nano-structures. Consequently, efficient and accurate methods are needed for the approximation and solution of the Liouville-von Neumann equation or Quantum-Liouville-type equations. For this purpose the discontinuous Galerkin (DG) approach is introduced, which already has been successfully applied in computational fluid dynamics [1].

Three main characteristics of the DG approach make it particularly suitable for this use case. Firstly, due to the discontinuous nature of the approximating functions, all resulting matrices are block diagonal. Hence, calculating the inverse of such matrices is computationally less demanding. Secondly, the inclusion of inverse matrices can be done during the early stages of discretization, where matrices are relatively small in dimension [2]. Lastly, with its underlying working principle on the basis of matrix-vector-multiplication, the DG approach is particularly suitable for the application in transient simulations as shown in [3]. These advantages make the DG method well suited for high-performance computing.

To establish a connection between the discontinuous finite elements, a numerical flux must be defined. The choice of the numerical flux, as well as the complex absorbing potential, have a major impact on the scheme's stability. Hence, investigating this influence is part of this work. To support the analysis of heterostructure devices, this work aims to expand the algorithm from [3] considering a spatially varying effective mass distribution and self-consistent Hartree potential in section II. In the same section, the algorithm is derived for the Liouville-von Neumann equation with a strong emphasis on the numerical flux and complex absorbing potential. The validation of the approach and the results are discussed in section III, followed by a conclusion in section IV.

II. FUNDAMENTALS

The DG method is utilized in conjunction with the Finite Volume Technique to approximate the Liouville-von Neumann equation (LVNE) in center of mass coordinates χ and ξ followed by an expansion in ξ-direction based on plane waves [3]. To expand this concept with a self-consistent Hartree potential and an inhomogeneous effective mass distribution, the Liouville operator of the LVNE is set up according to $\mathcal{L} = \mathcal{H}(z) - \mathcal{H}(z')$. The Hamiltonian $\mathcal{H}$ is defined as $\mathcal{H}(y)$ with z and z' as its coordinates

$$\mathcal{H}(y) = -\frac{\hbar^2}{2}\left\{\left(\frac{\partial}{\partial y}\right)\frac{1}{m(y)}\left(\frac{\partial}{\partial y}\right)\right\} + V(y). \quad (1)$$

Here $m(y)$ is the spatially varying effective mass. V contains the self-consistent Hartree potential, the band structure potential, and the contribution by the externally applied bias. Eventually, after simplifying the Liouville operator $\mathcal{L}$ and after a transformation into center-mass

coordinates according to $\chi = 1/2 \cdot (z + z')$ and $\xi = z - z'$, the LVNE can be rewritten as

$$\frac{\partial}{\partial t} \boldsymbol{\rho}(\chi, t) = \boldsymbol{D}_2(\chi) \frac{\partial^2}{\partial \chi^2} \boldsymbol{\rho}(\chi, t) + \boldsymbol{D}_1(\chi) \frac{\partial}{\partial \chi} \boldsymbol{\rho}(\chi, t)$$
$$+ \boldsymbol{D}_0(\chi) \boldsymbol{\rho}(\chi, t), \tag{2}$$

to include the second derivative $\partial^2/\partial \chi^2$ stemming from the spatially varying effective mass. The three expressions $\boldsymbol{D}_2$, $\boldsymbol{D}_1$, and $\boldsymbol{D}_0$ are obtained from the above mentioned Liouville operator $\mathcal{L}$ according to [4]

$$\boldsymbol{D}_2^{l,l'}(\chi) = \frac{\imath \hbar}{8} m_-(\chi, \xi_l) \cdot \delta_{l,l'}$$

$$\boldsymbol{D}_1^{l,l'}(\chi) = \frac{\imath \hbar}{4} \frac{\partial}{\partial \chi} m_-(\chi, \xi_l) + \frac{\imath \hbar}{2} m_+(\chi, \xi_l)$$
$$\cdot \left(\frac{\delta_{l,l'-1} - \delta_{l,l'+1}}{2\Delta\xi} \right)$$

$$\boldsymbol{D}_0^{l,l'}(\chi) = \frac{\imath \hbar}{2} \frac{\partial}{\partial \chi} m_+(\chi, \xi_l) \cdot \left(\frac{\delta_{l,l'-1} - \delta_{l,l'+1}}{2\Delta\xi} \right)$$
$$+ \frac{\imath \hbar}{2} m_-(\chi, \xi_l) \cdot \left(\frac{\delta_{l,l'-1} - 2\delta_{l,l'} - \delta_{l,l'+1}}{\Delta\xi^2} \right)$$
$$+ \frac{1}{\imath \hbar} \cdot \left(V(\chi + \frac{\xi_l}{2}) - V(\chi - \frac{\xi_l}{2}) - \imath W(\xi_l) \right).$$

The expression $m_\pm$ denounces the spatially varying effective mass in center-mass coordinates in accordance with the relationship

$$m_\pm(\chi, \xi) = \frac{1}{m(\chi + \xi/2)} \pm \frac{1}{m(\chi - \xi/2)}.$$

The Hartree potential as well as the complex absorbing potential (CAP) are found within the last summand of the operator $\boldsymbol{D}_0(\chi)$. The CAP shall be discussed at a later stage of this work. Next, a substitution is carried out by introducing

$$\boldsymbol{u}(\chi) = \frac{\partial}{\partial \chi} \boldsymbol{\rho}(\chi, t). \tag{3}$$

Then, inserting (3) in (2) yields the reduced first order LVNE defined as

$$\frac{\partial}{\partial t} \boldsymbol{\rho}(\chi, t) = \boldsymbol{D}_2(\chi) \frac{\partial}{\partial \chi} \boldsymbol{u}(\chi) + \boldsymbol{D}_1(\chi) \boldsymbol{u}(\chi)$$
$$+ \boldsymbol{D}_0(\chi) \boldsymbol{\rho}(\chi, t). \tag{4}$$

Ultimately, a system of two equations with (3) and (4) containing the two unknown vectors $\boldsymbol{u}$ and $\boldsymbol{\rho}$ results. Next, the conventional finite element formalism (FEM) with test functions $l_i(\chi)$ is introduced, eventually arriving at a notation with the stiffness- and mass matrix $\boldsymbol{S}$ and $\boldsymbol{M}$ typical for FEM as derived in [3]. However, the peculiarity of the discontinuous Galerkin method is the

non-overlapping characteristic of the one-dimensional finite elements resulting in block-diagonal matrices. That is, each element has three distinct nodes due to a quadratic ansatz in the χ-domain. The numerical flux is found in the first order derivatives $\partial/\partial\chi \boldsymbol{\rho}(\chi, t)$ and $\partial/\partial\chi \boldsymbol{u}(\chi)$ from (3) and (4), respectively. The density matrix $\boldsymbol{\rho}$ and the substitution function $\boldsymbol{u}$ are transformed into the eigenspace according to the transformation $\boldsymbol{c}(\chi, t) = \boldsymbol{\Phi}^\dagger \cdot \boldsymbol{\rho}(\chi, t)$ and $\tilde{\boldsymbol{u}}(\chi) = \boldsymbol{\Phi}^\dagger \cdot \boldsymbol{u}(\chi)$, respectively. For the transformation, a matrix $\boldsymbol{\Phi}$ is utilized containing the basis vectors column-wise corresponding to the eigenvalues λ_j derived from the expansion in the ξ-domain based on plane waves [4]. After performing a two-stage partial integration, the local strong formulation, as described in [3], is obtained utilizing Green's theorem. Both equations in their strong variant read as

$$\boldsymbol{M}^k \frac{\partial}{\partial t} \boldsymbol{c}_j^k - \boldsymbol{D}_2 \boldsymbol{S}^k \boldsymbol{f}_j^k + \boldsymbol{D}_1 \boldsymbol{M}^k \tilde{\boldsymbol{u}}_j^k + \boldsymbol{D}_0 \boldsymbol{M}^k \boldsymbol{c}_j^k$$
$$= \boldsymbol{D}_2 \oint_{\partial D^k} (u_j^k(\chi) - u_j^{k,*}(\chi) \hat{n} \underline{l}(\chi) \tag{5}$$

and

$$\boldsymbol{M}^k \tilde{\boldsymbol{u}}_j^k - \boldsymbol{S}^k \boldsymbol{f}_j^k = \oint_{\partial D^k} (f_j^k(\chi, t) - f_j^{k,*}(\chi, t) \hat{n} \underline{l}(\chi). \tag{6}$$

In both cases a numerical flux is introduced. To generate the values for the numerical fluxes, the right-hand-sides of (5) and (6) have to be evaluated. For demonstration purposes, it shall suffice to perform this step on (6). For simplicity, in both cases an upwinding flux is assumed, such that the right-hand-side of (6) would evaluate to

$$\oint_{\partial D^k} (f_j^k(\chi, t) - f_j^{k,*}(\chi, t)) \hat{n} l_i(x) =$$
$$\lambda_j \left(\frac{c_{r/l}^- + c_{r/l}^+}{2} \right) + |\lambda_j| \frac{1 - \alpha}{2} [[c]]_{r/l}. \tag{7}$$

Where $\left(c_{r/l}^- + c_{r/l}^+ \right)/2$ is the continuity, $[[c]]_{r/l}$ refers to the jump, which is further defined as $[[c]]_{r/l} = \hat{n}_{r/l}^- \cdot c_{r/l}^- + \hat{n}_{r/l}^+ \cdot c_{r/l}^+$. Concerning the notation, $\hat{n}_{r/l}^\pm$ denote vectors pointing to the interior $(^-)$ and to the exterior $(^+)$ of the right and left edge of each element, respectively. Additionally, λ_j denotes the eigenvalue of each element, and finally α describes the weight of the jump that is accounted for in the upwind flux. For further information on α, refer to Tab. I in section III.

Since $\boldsymbol{u}$ is spatially invariant at the boundaries of the computational domain, the numerical flux affecting $\boldsymbol{u}(\chi)$ does not contribute to the boundary conditions. As for the numerical flux affecting $\boldsymbol{\rho}(\chi, t)$, Dirichlet and inflow

boundary conditions are set corresponding to the Fermi-Dirac distribution [5], [7].

For the theoretical derivation of the LVNE, an infinitely expanding domain corresponding to the ξ-coordinate is assumed. This assumption is necessary such that the wave function disappears regarding infinity. However, due to the numerical approximation of the LVNE, this assumption opposes the need for the finiteness of each computational domain. Therefore, the termination of the ξ-domain with open boundaries causes the appearance of the values of the statistical density matrix ρ as additional surface terms. Contrary to this fact, it is common to neglect these surface terms in the common literature. From a mathematical viewpoint, this method corresponds to the formulation of zero valued Dirichlet boundary conditions for the density matrix in the space domain. From a physical viewpoint, the ξ-domain is now equipped with a perfectly reflecting layer at its edges. These reflections overlap with the original values of the density matrix distorting the numerical results. To counteract this problem, a complex absorbing potential is deployed, which represents a dampening layer at the said edges eliminating above mentioned reflections [5], [6].

After a subdivision of the computational domains Ω_χ and Ω_ξ into N_χ and N_ξ elements, with an order N for the approximating functions, the square system matrix has a dimension of $2N_\chi N_\xi (N+1)$.

III. NUMERICAL RESULTS

The DG method is validated on the basis of a resonant tunneling diode (RTD), which is schematically shown in Fig. 1. The physical dimensions and the numerical settings, including the upwind flux, are adopted from [3]. First, the result for the spatially varying effective mass distribution is compared with a homogeneous mass distribution for the steady state case and the thermal equilibrium in Fig. 1. Evidently, the density between the double barrier is higher with n_{mih}, which is in agreement with the results in [4]. For the transient simulation, each iteration is computed utilizing the fourth-order Runge Kutta algorithm. For a successful convergence of the scheme, the eigenvalues of the system matrix must be exclusively on the left of the complex plane. That is, their real part must be negative [8]. Fig. 2a presents the eigenvalues of the time dependent system matrix without the CAP, while Fig. 2b shows the eigenvalues with the CAP applied. The numerical flux deployed in this case is of an upwinding nature ($\alpha = 0$) as defined in section II. To further analyze the stability dependency
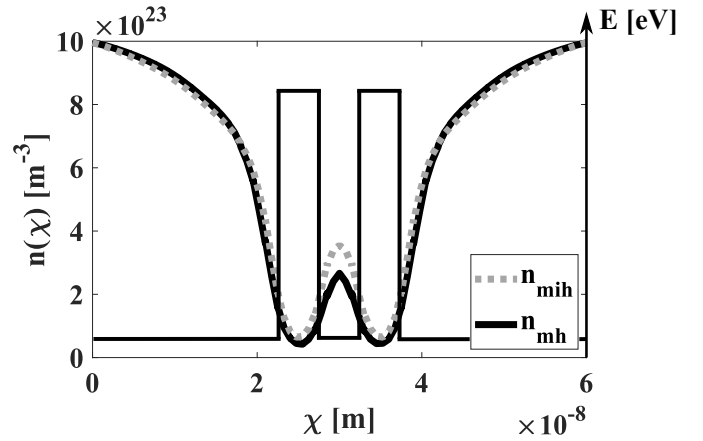

Fig. 1: Self-consistent carrier distribution in a RTD for a homogeneous n_{mh} and for an inhomogeneous effective mass distribution n_{mih}. The band edge energy E is added for clarity. The spatially varying effective mass distribution was chosen accordingly.
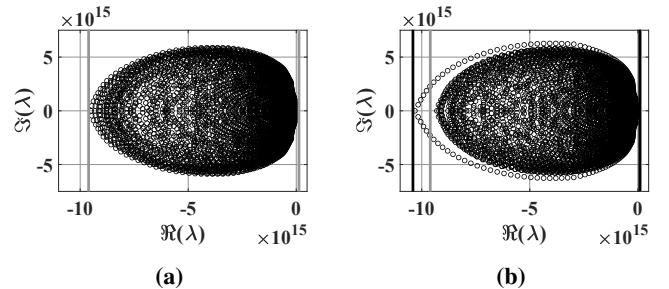

Fig. 2: Stability analysis for the upwind flux without the CAP (a) and with the CAP (b) showing the characteristic eigenvalues of the system matrix.

of the scheme on the numerical flux, Fig. 3a and Fig. 3b display the eigenvalue spectrum with a central flux ($\alpha = 1$), while Fig. 3c and Fig. 3d show a central flux, where the upwinding proportion is weighted with 50% ($\alpha = 0.5$). The central numerical flux does not take into account the direction of the propagating wave. Hence, it is to be expected that an upwind flux should produce better results.

Analogously to the investigation in Fig. 2a–2b, both

TABLE I: Maximum real part of the eigenvalues for different α without CAP ($\Re_{max}(\lambda_{nC})$) and with CAP ($\Re_{max}(\lambda_C)$). α is a constant between 0 and 1 linked to the weight of the upwinding flux, i.e. $\alpha = 1$ denotes a central flux, while $\alpha = 0$ represents an upwind flux.

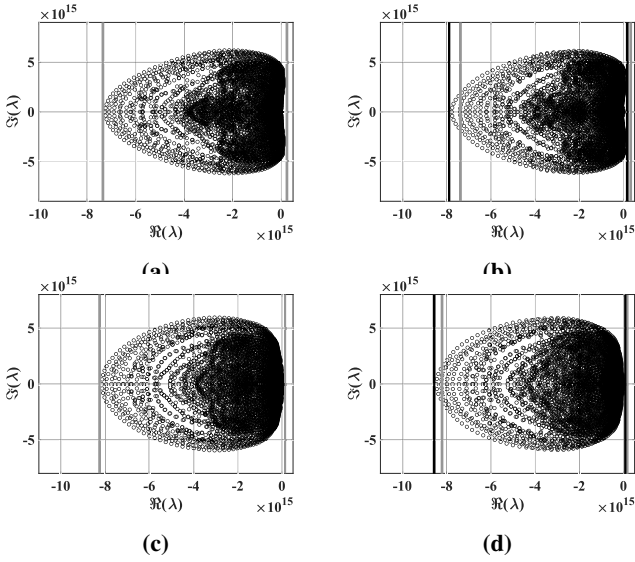| α	1.0	0.5	0.0
$\Re_{max}(\lambda_{nC})$	$0.0668 \cdot 10^{15}$	$0.0015 \cdot 10^{15}$	$-3.92 \cdot 10^{8}$
$\Re_{max}(\lambda_C)$	$0.0046 \cdot 10^{15}$	$-0.0011 \cdot 10^{15}$	$-0.0012 \cdot 10^{15}$

Fig. 3: Stability analysis for the central flux without the CAP (a) and with the CAP (b), as well as the weighted flux for $\alpha = 0.5$ without the CAP (c) and with the CAP (d) showing the characteristic eigenvalues of the system matrix.

Fig. 4: Time dependent carrier distribution n over the computational χ-domain, with a self-consistent Hartree potential and inhomogeneous effective mass distribution.

proposed numerical fluxes are analyzed with and without the CAP. To clarify the influence of the CAP on the eigenvalue spectrums provided in Fig. 2a–2b and Fig. 3a–3d, the maximum values of the real part for the previously mentioned numerical fluxes are examplarily calculated and summarized in Tab. I. As it can be seen from the gray and black vertical lines in Fig. 3c-3d, as well as the values from Tab. I, the eigenvalue spectrum of the weighted numerical flux ($\alpha = 0.5$) is shifted far enough to the left half of the complex plane, such that a stable algorithm is ensured. Therefore, it can be concluded that the CAP has a considerable positive impact on the stability of the proposed algorithm. A transient analysis can be thus undertaken as demonstrated in Fig. 4, in which a convergence beginning with the case for the thermal equilibrium leading to the thermal non-equilibrium case can be observed.

IV. CONCLUSION

Finally, the hybrid DG concept proposed in [3] has been successfully expanded to include the case of a spatially varying effective mass distribution, while showing good agreement with the results in [4]. Furthermore, it was proven that the deployment of a CAP can counteract the inherent stability issues of the DG approach introduced by the numerical flux, thus, optimizing the algorithm for time dependent analyses. The transien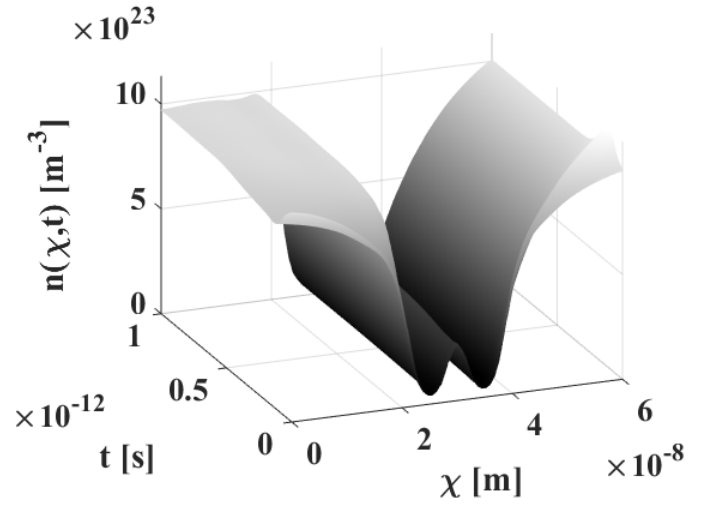t simulation with an inhomogeneous distributed effective mass successfully converged and provided a carrier distribution over time that complies with the common literature. As such, the DG approach is well suited to analyze nanoscale heterostructure devices avoiding the inherent stability issues by utilizing the CAP.

REFERENCES

[1] B. Cockburn, "Discontinuous Galerkin methods for computational Fluid Dynamics", *John Wiley And Sons, Ltd*, 2017, pp. 1-63, doi: https://doi.org/10.1002/9781119176817.ecm2053

[2] B. Cockburn, G. E. Karniadakis, C. W. Shu, "The Development of Discontinuous Galerkin Methods", 2000

[3] V. Ganiu, D. Schulz, "Discontinuous Galerkin concept for Quantum-Liouville type equations", *Solid-State Electronics*, vol. 200, p. 108536, 2023, doi: https://doi.org/10.1016/j.sse.2022.108536

[4] L. Schulz, D. Schulz, "Formulation of a phase space exponential operator for the Wigner transport equation accounting for the spatial variation of the effective mass", *J Comput Electron*, vol. 15, no. 5, pp. 801-809, 2016, doi: https://doi.org/10.1007/s10825-020-01551-0

[5] L. Schulz, D. Schulz, "Numerical Analysis of the Transient Behavior of the Non-Equilibrium Quantum Liouville Equation", *IEEE Trans. on Nanotech.*, vol. 17, no. 6, pp. 1197–1205, 2018, doi: 10.1109/TNANO.2018.2868972

[6] L. Schulz and D. Schulz, "Complex Absorbing Potential Formalism Accounting for Open Boundary Conditions Within the Wigner Transport Equation," in IEEE Transactions on Nanotechnology, vol. 18, pp. 830-838, 2019, doi: 10.1109/TNANO.2019.2933307.

[7] W. R. Frensley, "Boundary conditions for open quantum systems driven far from equilibrium", *Rev. Mod. Phys.*, vol. 62, no 3, pp. 745–791, Jul. 1990, doi: 10.1103/RevModPhys.62.745

[8] G. Fu, C.-W. Shu, "Optimal energy-conserving discontinuous Galerkin methods for linear symmetric hyperbolic systems", *J Comput Physics*, vol. 394, pp. 329–363, 2019, doi: https://doi.org/10.1016/j.jcp.2019.05.050